



UNIVERSITY OF LEEDS

This is a repository copy of *On the nature of cracks and voids in nuclear graphite*.

White Rose Research Online URL for this paper:

<http://eprints.whiterose.ac.uk/99603/>

Version: Accepted Version

Article:

Freeman, HM, Jones, AN, Ward, MB et al. (5 more authors) (2016) On the nature of cracks and voids in nuclear graphite. *Carbon*, 103. pp. 45-55. ISSN 0008-6223

<https://doi.org/10.1016/j.carbon.2016.03.011>

© 2016. This manuscript version is made available under the CC-BY-NC-ND 4.0 license
<http://creativecommons.org/licenses/by-nc-nd/4.0/>

Reuse

Unless indicated otherwise, fulltext items are protected by copyright with all rights reserved. The copyright exception in section 29 of the Copyright, Designs and Patents Act 1988 allows the making of a single copy solely for the purpose of non-commercial research or private study within the limits of fair dealing. The publisher or other rights-holder may allow further reproduction and re-use of this version - refer to the White Rose Research Online record for this item. Where records identify the publisher as the copyright holder, users can verify any specific terms of use on the publisher's website.

Takedown

If you consider content in White Rose Research Online to be in breach of UK law, please notify us by emailing eprints@whiterose.ac.uk including the URL of the record and the reason for the withdrawal request.



eprints@whiterose.ac.uk
<https://eprints.whiterose.ac.uk/>

On the nature of cracks and voids in nuclear graphite

H.M. Freeman¹, A.N. Jones², M.B. Ward¹, F. S. Hage³, N. Tzelepi⁴, Q.M. Ramasse³, A.J. Scott¹, R.M.D. Brydson^{1, 3}

¹ *Institute for Materials Research, School of Chemical and Process Engineering, Univ. Leeds, LS2 9JT*

² *Nuclear Graphite Research Group, Materials Performance Centre, Univ. Manchester, M13 9PL*

³ *SuperSTEM Laboratory, SciTech Daresbury Laboratories, Daresbury, WA4 4AD*

⁴ *National Nuclear Laboratory, Central Laboratory, Sellafield, CA20 1PG*

Abstract

Microcracks in neutron-irradiated nuclear grade graphite have been examined in detail for the first time using a combination of transmission electron microscopy (TEM), electron energy loss spectroscopy (EELS), energy dispersive X-ray (EDX), and energy filtered TEM (EFTEM). Filler particles from both unirradiated Pile Grade A (PGA) and three irradiated British Experimental Pile 'O' (BEPO) graphite specimens were investigated with received doses ranging from 0.4 to 1.44 displacements per atom (dpa) and an irradiation temperature of between 20-120°C. We suggest that the concentration and potentially the size of microcracks increase with increasing neutron irradiation and show that disordered carbon material is present in a range of microcracks (of varying size and shape) in all specimens including unirradiated material. EFTEM and EELS data showed that these cracks contained carbon material of lower density and graphitic character than that of the surrounding bulk graphite. The presence of partially filled microcracks has potentially significant implications for the development of microstructural models for the prediction of radiation-induced dimensional and property changes in nuclear graphite.

1. Introduction

The majority of the UK's operating nuclear reactors contain significant levels of graphite which not only moderates the energies of fast neutrons due to the high scattering cross section, but provides structural support, accommodates fuel and control rods, and allows for coolant flow. High levels of neutron irradiation and temperature result in chemical and physical property changes which consequently affect the structural integrity and functionality of the channel which would affect the safe running of the reactor. The reactor lifetime is therefore limited by the condition of the irreplaceable graphite, so an understanding of its behaviour is essential for plant safety and maximised power output.

Nuclear graphite consists of a coke-based filler, filler-binder matrix, and voids. The voids are in the form of gas-escape pores and cracks of varying dimension accounting for ca. 20% of the total volume. This graphite composite is often imparted with a preferred orientation via extrusion which assumes the filler crystallites (particularly if they are needle shaped) are aligned with their *c*-axes perpendicular to

the extrusion direction. The removal of volatiles during the manufacturing process produces gas-escape pores which are open and do not accommodate thermal expansion due to their larger dimension [1]; however they do affect properties such as strength, thermal conductivity and Young's modulus, particularly under radiolytic oxidation during reactor operation [2]. Gas-escape pores have therefore not been considered in this study.

During almost every step in the high temperature graphitisation process associated with the manufacture of nuclear graphite and also during reactor operation, cracks arise due to a number of factors. Firstly, as a result of gradients in both temperature (during manufacture and operation) and neutron flux (during operation) and, secondly, as a result of the anisotropy of the coefficient of thermal expansion (CTE) in crystallites and the consequent generation of internal stresses beyond the elastic limit of graphite crystals [3–5]. The internal stresses act on both the carbon bonds between crystallites and on the Van der Waals forces between basal planes; to relieve this stress cracks form, more usually between the weaker bound basal planes. Since the CTE is higher in the crystallographic *c*-direction (ca. $20 - 40 \times 10^{-6} \text{ K}^{-1}$ compared to $< 1.5 \times 10^{-6} \text{ K}^{-1}$ in the *a*-direction), lenticular cleavage cracks between basal planes, known as Mrozowski (micro)cracks, are observed to form lying approximately perpendicular to the crystallographic *c*-direction as a result of anisotropic contraction following post graphitization cooling during manufacture [2–4].

The basic understanding of irradiation-induced dimensional change in a perfect graphite crystal involves growth in the *c*-axis and contraction in the *a*-axis. This is presumed to arise from the formation of interstitial and vacancy defects during neutron bombardment which can accumulate as clusters. However the microstructure of nuclear graphite is complex and at low doses, it is suggested that *c*-axis expansion is accommodated by the microcracks [3,6] leaving solely to shrinkage along the *a*-axis which leads to the observed net volume shrinkage. With increasing dose during reactor operation, the rate of contraction or shrinkage reduces and eventually the cracks are presumed to close and *c*-axis expansion is no longer accommodated producing net volume expansion, the critical point at which this reversal occurs is known as “turnaround” which can vary with operating temperature [7].

Microcracks can be classified into two categories: intra and inter-granular, where the former are found within crystallites and lie perpendicular to the crystallographic *c*-direction (e.g. Mrozowski cracks [2,4]). The latter lie between crystallites at grain boundaries with, in principle, no specific orientation with respect to neighbouring basal planes, unless crystallites are aligned as a result of mesophase development. Within thermally anisotropic filler particles, (closed) calcination cracks form due to volumetric shrinkage during the 1300°C calcination stage in the manufacturing process [3].

In nuclear graphite, microcracks have been reported to range in size from less than ca. 5nm to 200nm in width and up to 10µm in length [2–4,6]. The nature of the material within a crack depends on the

crack type; it has been proposed that microcracks in Pile Grade A, Gilsocarbon, baked carbon [6], and highly ordered pyrolytic graphite (HOPG) [6,8] contain low density disordered carbon perhaps arising from interstitial atoms migrating from the bulk following irradiation and sintering-induced diffusion. However, limited research has been carried out to characterise this material in both non-irradiated and irradiated graphite, which could better the understanding of the mechanisms involved in crack expansion and contraction [2,8], and hence their influence on macroscopic properties such as CTE and elastic modulus during reactor operation.

Delannay *et al.* [5] used crystal plasticity finite element modelling to predict irradiation-induced dimensional change and variations in CTE at a variety of reactor temperatures. Predictions were in agreement with experimental data showing bulk material shrinkage with irradiation and turnaround after crack closure. All cracks in this model were empty; extending the model to 3D and including a proportion of filled cracks could be of interest in relation to the results subsequently described in this paper.

The investigation of a variety of microcracks in non-irradiated nuclear graphite and HOPG has been undertaken by Wen *et al.* [6] who showed the presence of lenticular cracks of up to 10 μ m long and up to 100nm wide in Pile Grade A (PGA) nuclear graphite; a fine structure of smaller cracks was also observed with crack lengths down to 10nm. Both empty and filled microcracks were identified in non-irradiated and electron irradiated material; cracks in the latter were suggested to contain low density, amorphous material. Via a comparison of transmission electron microscope (TEM) samples produced by both ion beam thinning and microtome sectioning techniques, it was confirmed that this amorphous material observed within the cracks was not a result of TEM sample preparation. In-situ heating of samples to 800 $^{\circ}$ C under a 200kV electron beam showed a gradual closure of cracks along the *c*-axis. Electron beam exposure without in-situ heating also caused cracks to close; after 15 minutes a 60nm crack was observed to reduce in width to 6nm, and in some areas to close completely.

Neutron irradiated nuclear graphite was also investigated by Karthik *et al.* [9], who used TEM to observe changes in both the microcracks and the nanostructure. In both filler and binder phases of NBG-18 and IG-110 graphites irradiated to 1.42 dpa and 1.91 dpa respectively, there were no significant changes in the size distribution of microcracks as compared to non-irradiated specimens. The absence of microcracks in specimens irradiated to ca. 6.7 dpa at ca. 670 $^{\circ}$ C was attributed to the closure of pre-existing microcracks from significant *c*-axis swelling. Open microcracks within filler particles in all specimens appeared to contain amorphous carbon but no further analysis on this material was performed. TEM lattice images of specimens irradiated to 6.78 dpa at 678 $^{\circ}$ C provided evidence for intense nanostructural damage through the fragmentation and bending of basal planes, however the retention of (002) spots in selected area electron diffraction (SAED) patterns showed that the layered

structure was preserved. Noise filtering of lattice images was used to highlight extended interlayer defects and prismatic dislocations, similar to those found following electron irradiation [10,11].

This paper extends this work and presents a study of microcracks in irradiated graphite samples removed from the British Experimental Pile 'O' (BEPO) reactor as well as in non-irradiated Pile Grade A (PGA) graphite for comparative purposes. Using TEM, energy dispersive X-ray spectroscopy (EDX), electron energy loss spectroscopy (EELS) and energy filtered TEM (EFTEM), the material within a variety of cracks is characterised in detail and suggestions are made regarding its origin and importance for understanding radiation-induced property changes in these materials. The material investigated in this work has also been studied using Raman spectroscopy by Krishna *et al.* [12], and the present results are correlated with their findings.

2. Experimental procedure and sample preparation

The nuclear graphite grades examined were BEPO and PGA; three BEPO samples of varying received dose were used from the same trepanned column. BEPO1 was farthest from the reactor core and received a dose of 0.4 dpa ($\approx 3.1 \times 10^{20}$ n cm⁻²), BEPO16 was in the middle of the channel and received a dose of 1.27 dpa ($\approx 9.8 \times 10^{20}$ n cm⁻²), whilst BEPO20 was closest to the core and received a dose of 1.44 dpa ($\approx 1.1 \times 10^{21}$ n cm⁻²). The irradiation temperature during operation (in air) was between 20°C and 120°C, which is lower than the usual advanced gas cooled reactor operating temperature of ca. 350°C. During the last 5 years the air was recirculated and temperatures were increased up to ca. 180°C to achieve a higher thermal output. The reactor was also annealed twice to ca. 230°C, once during operation and once after to release the 200°C Wigner peak [13]. BEPO graphite is an extruded coke-based grade containing elongated needle filler particles (similar to those found in PGA) within a porous binder phase where the binder and crystallites do not have preferential alignment. The filler particles are fairly consistent in size, of the order 1mm × 0.5mm [14]. The BEPO reactor was in operation from 1948-1968 at Harwell in the UK and used natural or low-enriched uranium fuel and a graphite moderator to demonstrate the design for the Windscale Piles and to provide a facility for materials testing and radioisotope production [15]. For comparison, a non-irradiated PGA graphite specimen was also studied. It is believed that there is no remaining non-irradiated BEPO graphite. Specimens for transmission electron microscopy (TEM) were prepared using an FEI Nova200 dual beam SEM/FIB fitted with a Kleindiek micromanipulator for in situ lift out. Using this sample preparation technique allowed for areas of filler to be specifically selected. The analysed areas had varying thickness; but always below 150nm. A gallium ion beam energy of 30kV and beam currents between 5000nA and 100nA were used, except for the final cleaning step where an energy of 5kV and current of 29pA were used in order to minimise the effects of beam damage and redeposition of sputtered material.

General TEM observations were carried out on an FEI Tecnai TF20 operated at 200kV. To avoid significant electron beam damage, images were focused away from the area of interest; the sample area was then moved to the site of interest and data then captured swiftly. EFTEM data was collected on a Philips CM200 operated at 200kV and fitted with a Gatan Imaging Filter (GIF) 200. The energy resolution was 0.7eV. EFTEM image acquisition was performed with a window width of 3eV (smallest available for plasmon mapping) and a collection angle defined by the objective aperture of 10.9mrad. The dose rate for experiments was of the order 10^4 electrons $\text{nm}^{-2} \text{s}^{-1}$. Images and spectra were captured with the 1 megapixel slow scan CCD array of the GIF. Data from the array were processed using Gatan's Digital Micrograph software. STEM/EDX measurements were carried out using an Oxford Instruments INCA 350 EDX system (probe size 5-10nm). EELS data was collected at SuperSTEM (the UK national facility for aberration corrected scanning TEM) using a Nion UltraSTEM100 equipped with a Gatan Enfina Spectrometer, operated at an acceleration voltage 60kV. The choice of operating voltage was made with the aim to minimize beam induced irradiation damage. The energy resolution in best conditions was 0.45eV and the convergence semi-angle was ca. 30mrad.

In order to measure and compare the density and graphitic nature of material within a microcrack to those of the bulk, EEL spectra were collected from several regions: within a microcrack, on the edge of a microcrack and in the neighbouring graphite bulk. Quoted energies from EEL spectra were determined by taking a first derivative to define the edge onset or peak position. Within the low loss region of a graphitic EEL spectrum, the π plasmon, around 6eV, provides information about the graphitic character, crystallinity and the degree of π bonding, and the $(\pi+\sigma)$ plasmon peak, at 26-27eV, is related to the valence electron density which can be related to the bulk density [16].

To determine stable conditions for such measurements which are independent of specimen orientation or experimental conditions, two calibration experiments were performed: the first monitored the change in $(\pi+\sigma)$ plasmon peak position with EELS collection semi-angle to establish the collection semi-angle threshold required for a non-variable plasmon peak position, and the second verified the orientation independence of the plasmon peak position at a specified collection angle (Figure 1). At 200kV the (magic angle) collection conditions were determined and published by Daniels *et al.* [17] for the microscopes used in these TEM experiments. For the EELS measurements at 60 kV, although the conditions did not satisfy the magic angle criterion, there was found to be only a small variation in plasmon peak position within a limited tilt range. Assuming there is no significant change in local orientation in the graphitic planes surrounding the cracks, any effect on the low loss spectrum should therefore be negligible. Furthermore, compared to the bulk material, it is expected that the material within the crack is more isotropic which would lead to a reduced effect of relative orientation changes in the spectrum.

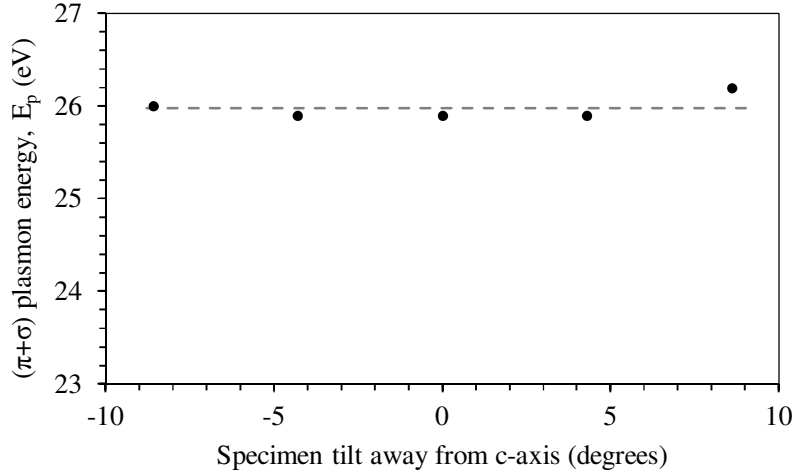


Figure 1 Change in ($\pi+\sigma$) plasmon peak position with specimen tilt ($\beta = 3.7\text{mrad}$) for an operating voltage of 60kV.

Preliminary EELS calibration studies showed that the ($\pi+\sigma$) plasmon peak energy position increased with increasing collection semi-angle (controlled by changing the camera length in diffraction mode) up to a limiting value of 26.5eV for a collection semi-angle of 3.4mrad at 60kV accelerating voltage; corresponding values for 80kV and 200kV were 4.0mrad and 7.6mrad respectively. For example, Figure 1 shows there is no significant variation in the ($\pi+\sigma$) plasmon peak energy with sample orientation for a collection semi-angle of 3.7mrad for 60kV over an angular (tilt) range of ca. 15 degrees similar to the results of Daniels *et al.* at 200kV [17]. Therefore, operating at a collection angle of $> 3.7\text{mrad}$ at 60kV during EEL spectroscopy ensures a consistency in plasmon peak position, where any changes are a direct result of varying density. The objective aperture used in the EFTEM plasmon ratio imaging at 200kV gives a collection angle of 10.9mrad and therefore satisfies the above condition that $\beta > 7.6\text{mrad}$ for 200kV. In the carbon K-edge core loss EEL spectra information about the planar sp^2 content and graphitic nature of the material can be determined from the π^* and σ^* peaks, around 285eV and 290eV respectively. In addition to the primary π^* peak at 285eV, the spectral intensity around 287eV gives information about hetero-atom content (deemed to be negligible in this case due to the high graphitization temperatures) and what we term as *non-planar* sp^2 carbon (non six membered rings which induce curvature in the basal planes) [11,18,19].

3. Results and discussion

Figure 2 shows TEM images of the FIB sections from the non-irradiated PGA and all three irradiated BEPO specimens. Image analysis of TEM micrographs showed that with increasing dose the (areal) concentration, width and periodicity of cracks appears to increase significantly and that all specimens (both non-irradiated and irradiated) contained both filled and empty cracks; the latter are evident in Figure 2(a-d) as regions of high intensity. This increase in the proportion of cracks within the material

reflects the fragmentation of the graphite microstructure with increasing neutron irradiation as has been observed in [20–22]. The periodicity (in cracks/ μm) and areal concentration (in % area) varied from: 4.5 and 1.5% in non-irradiated PGA; to 0.21 and 1.0% in BEPO1; 0.56 and 4.4% in BEPO16 and 1.70 and 9.6% in BEPO20, respectively. PGA showed many long narrow cracks which were ca. 10 nm wide and up to $1\mu\text{m}$ long. BEPO1 showed slightly wider cracks (ca. 50-300nm), BEPO16 showed considerably wider cracks, whilst BEPO20 showed a mixture of long thin lenticular cracks and larger wide cracks. Despite all specimens being selected from filler regions, we appreciate that such observations and semi-quantitative analysis must be interpreted with caution owing to the heterogeneous nature of nuclear grade graphite.

In Figure 3, higher magnification TEM images show a range of microcracks (labelled A-D). In the TEM bright field micrograph in Figure 3(b) regions of darker contrast might refer to either thicker material or material of a higher graphitic content. To distinguish between the two, EFTEM images were also collected and plasmon ratio maps were produced, the results of which will be discussed later in this section. High magnification TEM imaging and electron diffraction provide information about the crystallographic orientation of the cracks, and from Figure 3(b) and (c) it is clear to see that the basal planes and cracks are aligned suggesting that these are intra-granular cracks within the same crystallite.

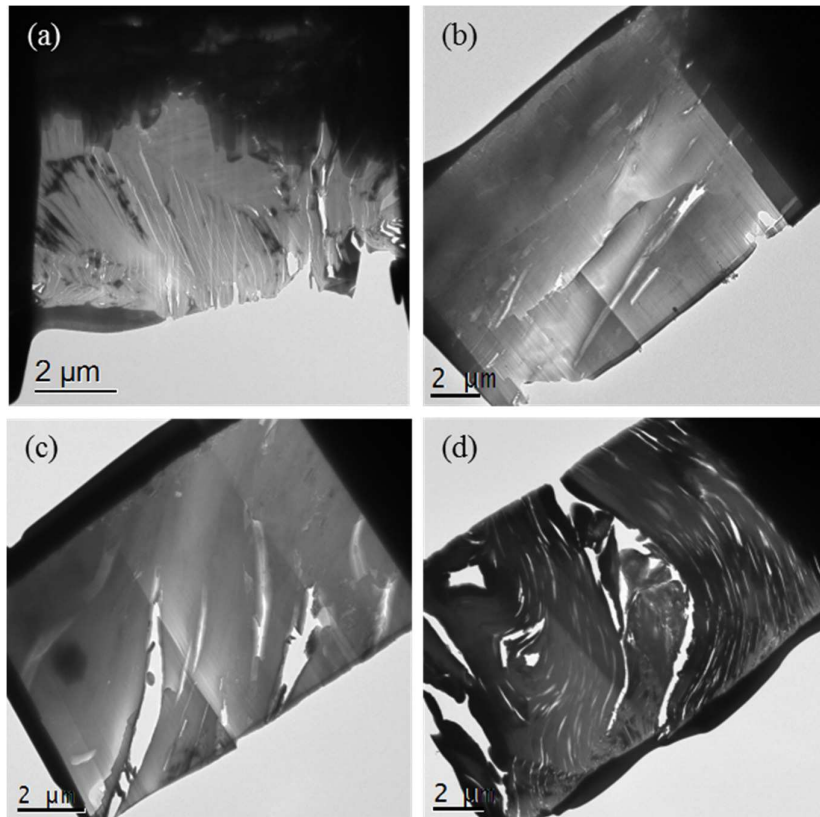


Figure 2 TEM images of a FIB section of filler from each sample: (a) non-irradiated PGA, (b) BEPO1, (c) BEPO16 and (d) BEPO20.

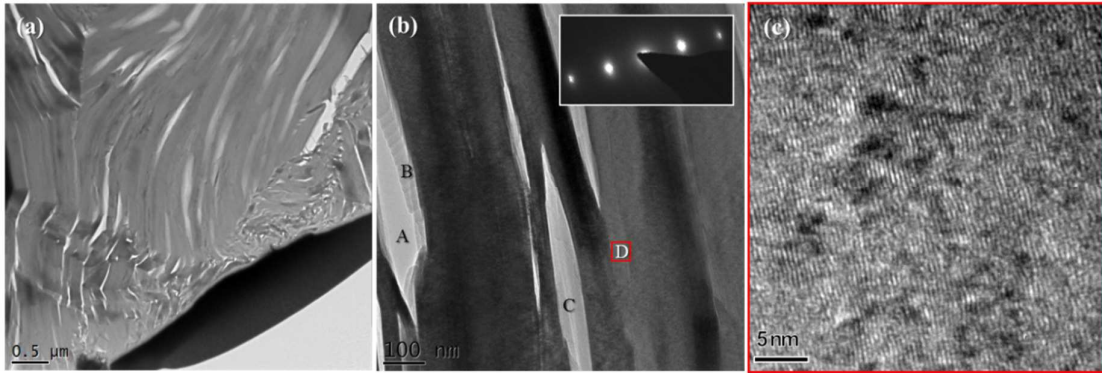


Figure 3 (a) relatively low magnification and (b) medium magnification TEM images of intra-granular microcracks within the FIB section of specimen BEPO20. Labels in (b): A - no material within the crack; B - material at the crack interface; C - a completely filled crack; D - graphitic bulk material. Electron diffraction pattern of the area shown in micrograph (b) is presented in the top right corner. (c) shows a high magnification TEM image of region D to verify the basal plane orientation is parallel to cracks.

To first establish that the material observed within a microcrack does not contain redeposited material from the FIB sputtering process or material amorphised by (Ga) ion beam implantation, EDX measurements were collected and quantified in terms of their Ga and Pt content (Figure 4). 15 EDX spectra were analysed; the Ga and Pt content of regions containing FIB induced material were found to be significantly higher (Figure 4). The low Ga and Pt content regions consistently contained below 0.2% Ga and 0.15% Pt (atom%); in our experience these are close to the limits of detection for these elements using this experimental setup. EDX spectra showing microcracks with Ga content $> 0.2\%$ and Pt content $> 0.15\%$ were therefore considered to contain FIB-induced damaged and/or redeposited material and all associated datasets were disregarded. The presence of a Cu peak in all spectra is due to the Cu TEM grid used, and the Pt peak which appears together with Ga is associated with FIB sputtering (from a protective Pt strap layer on top of the specimen) and redeposition. The small levels of Ga visible in Figure 4 (a) are most likely due to an unavoidable Ga implantation outer layer associated with all FIB prepared samples [23]. Specifically we note that, firstly, all samples studied (including unirradiated material) contained both filled and empty cracks in agreement with the findings of Wen *et al.* [6] for unirradiated material and Karthik *et al.* [9] for neutron irradiated material – in both cases samples having been prepared by conventional ion beam thinning (and also microtomy in the case of Wen *et al.* [6]). Secondly, in the irradiated material, shown for example in Figure 4(a), we observed the presence of filled microcracks which were not associated with significant levels of Ga. When taken together this suggests that our FIB preparation protocol is relatively robust in relation to redeposition of sputtered material and also significant amorphisation.

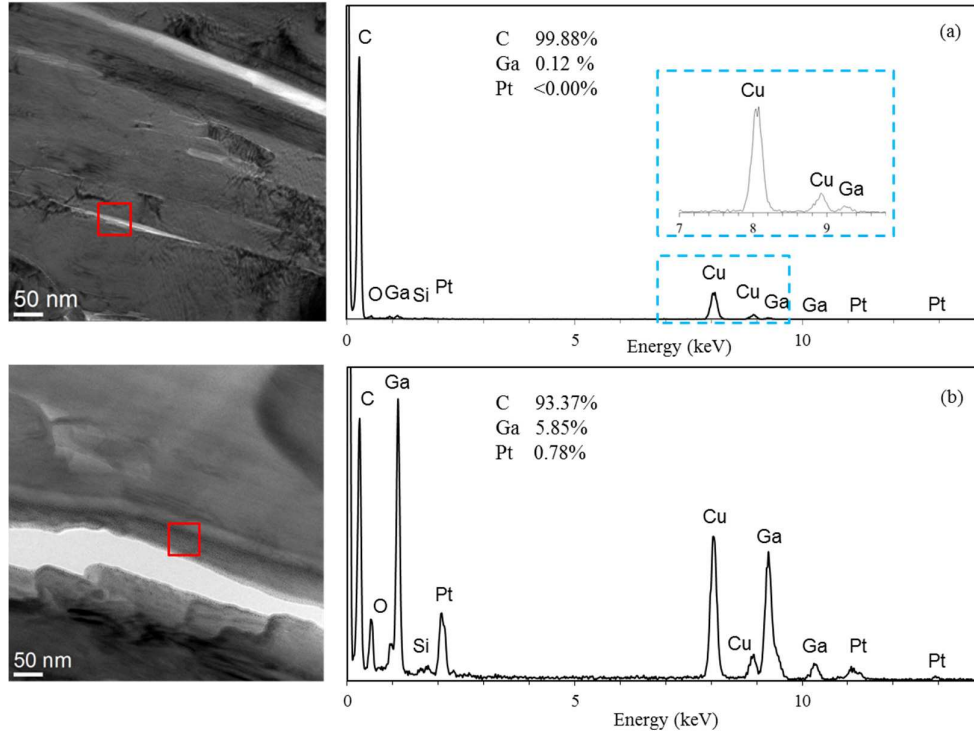


Figure 4 Examples of EDX spectra over a crack in BEPO1 showing (a) negligible Ga content (0.12%) and (b) significant Ga content (5.85%). Both spectra were normalised to the carbon peak at 0.2774keV.

EFTEM images were also used to assess the graphitic nature of the material within a microcrack. Following the procedure outlined in Daniels *et al.* [17], two filtered images were used to produce an $I_{27\text{eV}}/I_{22\text{eV}}$ plasmon ratio map to remove diffraction contrast and thickness effects; a 3eV window centered at 27eV representing the position of the plasmon peak for graphite and a 3eV window centered at 22eV representing the position of the plasmon peak for non-graphitized material. Ratio maps were calibrated to $0.8 \leq I_{27\text{eV}}/I_{22\text{eV}} \leq 1.8$ following measurements by [17] so that high intensity reflects graphitic material and low intensity non-graphitic material.

To confirm the removal of thickness contrast, this method was first applied to a HOPG specimen of varying thickness (Figure 5). Here it can be seen that significant thickness contrast in the unfiltered TEM image of HOPG translates to relatively even contrast in the plasmon map; whilst the amorphous carbon support film appears much darker due to the lack of graphitic character. In Figure 5(b) the plasmon ratio intensity drops linearly from 1.4 to 0.6 at the HOPG surface indicating a presence of amorphous carbon. The plasmon ratio intensity over the hole is negligible which should be taken into account when analysing the material/lack of material within a microcrack in an EFTEM of irradiated graphite. The degree of success in thickness contrast removal is dependent on the symmetry of the $(\pi+\sigma)$ plasmon; according to Daniels *et al.* [17] significant asymmetry which might affect the plasmon maps

occurs for sample thicknesses over ca. 200nm. The thickness of each area was therefore determined (using EELS) to ensure this criterion was satisfied.

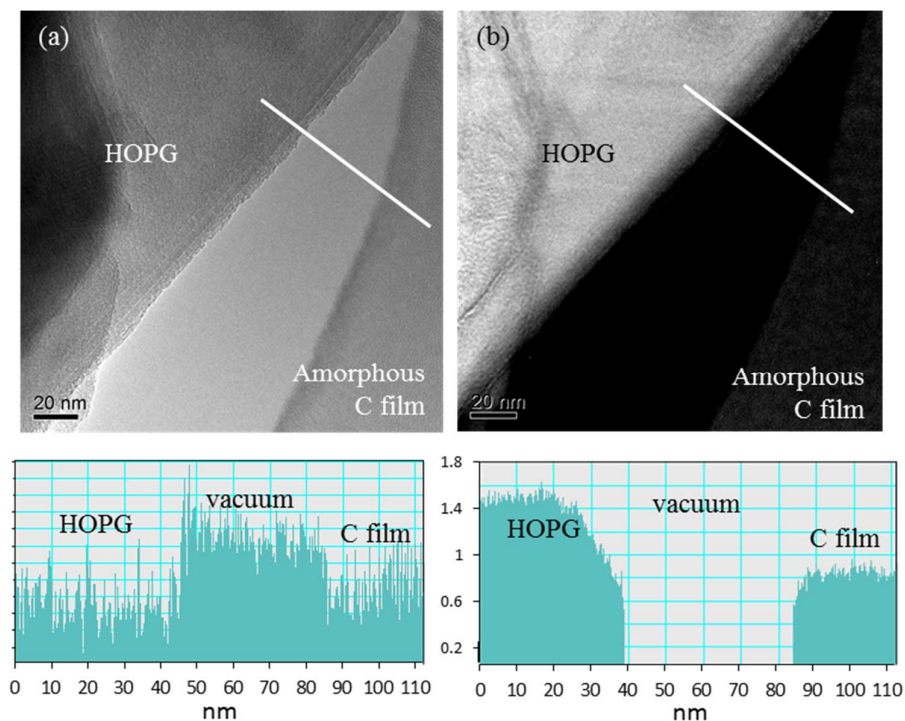


Figure 5 (a) TEM image of HOPG and amorphous carbon film (as labelled) showing thickness contrast on the left hand side of the region of HOPG. (b) EFTEM $I_{27\text{eV}}/I_{22\text{eV}}$ plasmon map showing a removal of significant thickness contrast. Intensity profiles of each image are shown below to illustrate the change in contrast (following the white intersections in the micrographs). TEM operating voltage 80kV in order to minimize beam damage.

The results of the EFTEM measurements on neutron irradiated BEPO specimens are shown in Figure 6 where the removal of thickness contrast is apparent when comparing the intensities in the zero loss, 22eV and 27eV filtered TEM images to the $I_{27\text{eV}}/I_{22\text{eV}}$ plasmon ratio map.

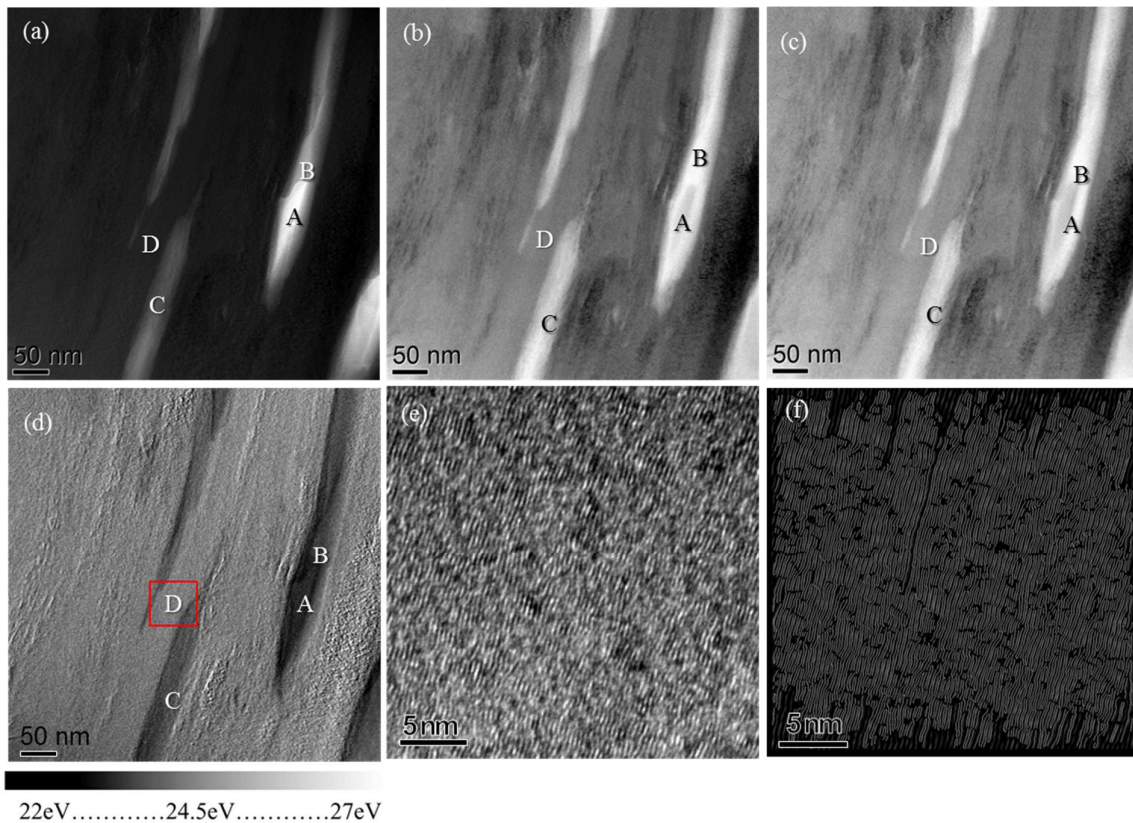


Figure 6 Representative EFTEM images for microcracks (A,B,C) in BEPO20. (a) zero loss filtered EFTEM, (b) 22eV filtered EFTEM, (c) 27eV filtered EFTEM, (d) $I_{27\text{eV}}/I_{22\text{eV}}$ plasmon ratio map with calibrated intensity scale below, (e) region of interest D in (d) showing graphitic material in the bulk between two cracks where the crack length and a -direction (002) are parallel, and (f) presents (002) fringe analysis of region of interest D.

Figure 6 shows a series of EFTEM (a-d), HRTEM (e), and the results of HRTEM image analysis (f) images from a FIB section of BEPO20. Four to six regions were analysed per BEPO specimen, the results shown in Figure 6 being representative. Four regions of interest have been identified in (a)-(d): three different areas within cracks (A-C) and part of the bulk between cracks (D). Figure 6(e) shows the basal planes in the graphitic bulk and (f) shows analysis of this micrograph to detect and measure fringe lengths and their tortuosity using software provided by the PyroMaN research group at the University of Bordeaux [24]. Analysis of (002) fringes in a variety of regions (>5 regions per specimen) for all three specimens highlights the effects of neutron radiation damage; fringes appear to be broken up (to lengths < ca.10nm) and tortuous (to levels of <1.14, the ratio of the length of the curve to the direct distance between two end points). There does not appear to be any specific correlation between fringe length/tortuosity and received dose however, suggesting the effects of neutron irradiation at the atomic scale are highly variable and site specific. A detailed discussion of this methodology and its application to nuclear graphite can be found in [11,24,25].

In Figure 6(a) the dark features in the zero loss EFTEM image represent thicker material whereas the inverse is the case for the 22eV and 27eV filtered images in (b) and (c). However in the plasmon ratio map (Figure 6(d)), the removal of thickness contrast means that bright features now represent regions of high graphitic character (27eV) and dark features reflect either a hole or a region of low graphitic character (22eV). Intensity profiles can be used to quantify interpretations (Figure 7). When comparing the zero loss EFTEM image (Figure 6(a)) to the plasmon ratio map (Figure 6(d)), regions A, B, and C clearly differ. In the zero loss EFTEM, the crack at region A shows a high intensity. This is mirrored in the plasmon ratio map, where a relatively low intensity is recorded (ca. 1.35 calibrated intensity units or 25.5eV). For region B in the same crack, the zero loss EFTEM image shows a slightly lower intensity which is matched with a higher intensity in the plasmon ratio map (ca. 1.45 calibrated intensity units or 26.3eV). The differences in plasmon ratio map intensities are shown in more detail in Figure 7 and particularly highlight the effects of thickness contrast. In the zero loss image, one might assume region A was a hole. However upon closer inspection in the plasmon ratio map both regions A and B contain low density graphitic material. The intensity and corresponding plasmon energy over different cracks in all EFTEM plasmon ratio maps were measured. The average plasmon intensity was 25.4eV; the lowest value was found over a crack in BEPO20 measuring 23.7eV and the highest over a crack in BEPO1 measuring 26.7eV.

On examination of the higher intensity regions in Figure 7, particularly that on the left of region B, a fluctuation in intensity with a periodicity of approximately 8nm suggests bands of material with different graphitic character are present; a result which is representative of all samples (with a slight variation of a few nm in periodicity). The change in intensity of these bands is reasonably significant with troughs as low as ca. 1.55 and peaks as high as ca. 1.75. These fluctuations are not a result of noise, the frequency of which is much higher. It is possible that these bands show the beginnings of crack formation where a trough (in the plasmon ratio map) will deepen and widen to form a crack containing disordered carbon. Damage accumulation and interstitial surface diffusion could perhaps result in regions of localised disordered material which act as sinks for further damage and eventually expand into cracks. A detailed discussion of the mechanisms for defect diffusion in graphite can be found in [26–29]. In general, diffusion along the basal plane is more common due to anisotropic atomic binding. It must be noted that the BEPO reactor operating temperature (20-120°C) is below the usual graphite moderated reactor operating temperature (>350°C) which may have hindered defect mobility. However, the reported migration energies of single vacancies and interstitials (created as a result of irradiation) vary considerably. Trevethan *et al.* [28] calculated ca. 1.1eV and 2eV for single vacancies and interstitials respectively (from DFT calculations), whereas Gulans *et al.* [27] calculated much lower interstitial migration energies of ca. 0.3eV based on unbound interstitial configurations. In both these publications, the calculated migration energies were related to temperature using the Arrhenius formula,

assuming a commonly used vacancy occurrence rate of 100/second and a defect vibrational frequency of 10^{14} Hz [27,28]. This analysis implies that a vacancy migration energy of 1.1 eV would correspond to a temperature of approximately 180°C. The low basal surface energy barrier ($1.06 \text{ meV}\text{\AA}^{-2}$ [30]) and the increase in nanocrystallinity following irradiation may create more possibilities for surface and grain boundary diffusion which would be expected to occur at much lower temperatures.

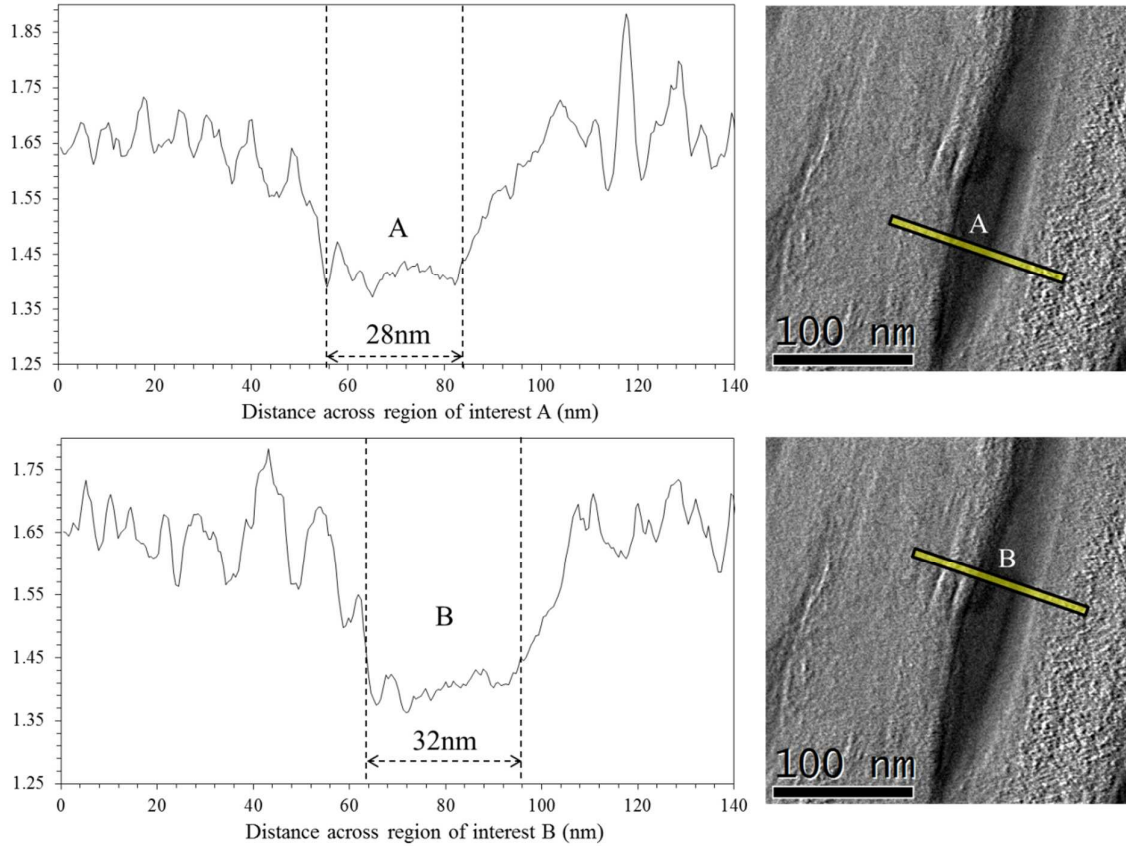


Figure 7 Intensity profiles across regions A and B from Figure 6 (d) plasmon ratio map to highlight differences in graphitic nature.

Having established stable EEL spectra collection conditions (as discussed in section 2), the variation in plasmon energy within and on the edge of a microcrack and in the neighbouring graphite bulk was measured using STEM/EELS spectrum imaging, as shown in Figure 8. For each area investigated high and medium angular annular dark field (HAADF/MAADF) images were acquired and then HAADF, MAADF and EELS spectrum images were collected from a specific region of interest. 0.68-6.2nm wide line scans of the EELS spectrum image were used to measure the energy position of the $(\pi+\sigma)$ plasmon, π plasmon peak, and the intensity of the π plasmon. Hyperspy was used to fit Gaussians to the two plasmon peaks and extract the required information (Figure 9) [31]. A fitting of a typical low loss spectrum using Gaussian peaks is shown in Figure 9; the following constraints were used:

- π plasmon Gaussian centred at ca. 6.25eV (with a constraint on the FWHM (β): $0.25\text{eV} \leq \beta \leq 6\text{eV}$);
- $(\pi+\sigma)$ plasmon Gaussian centred at ca. 25eV ($10\text{eV} \leq \beta \leq 17\text{eV}$).

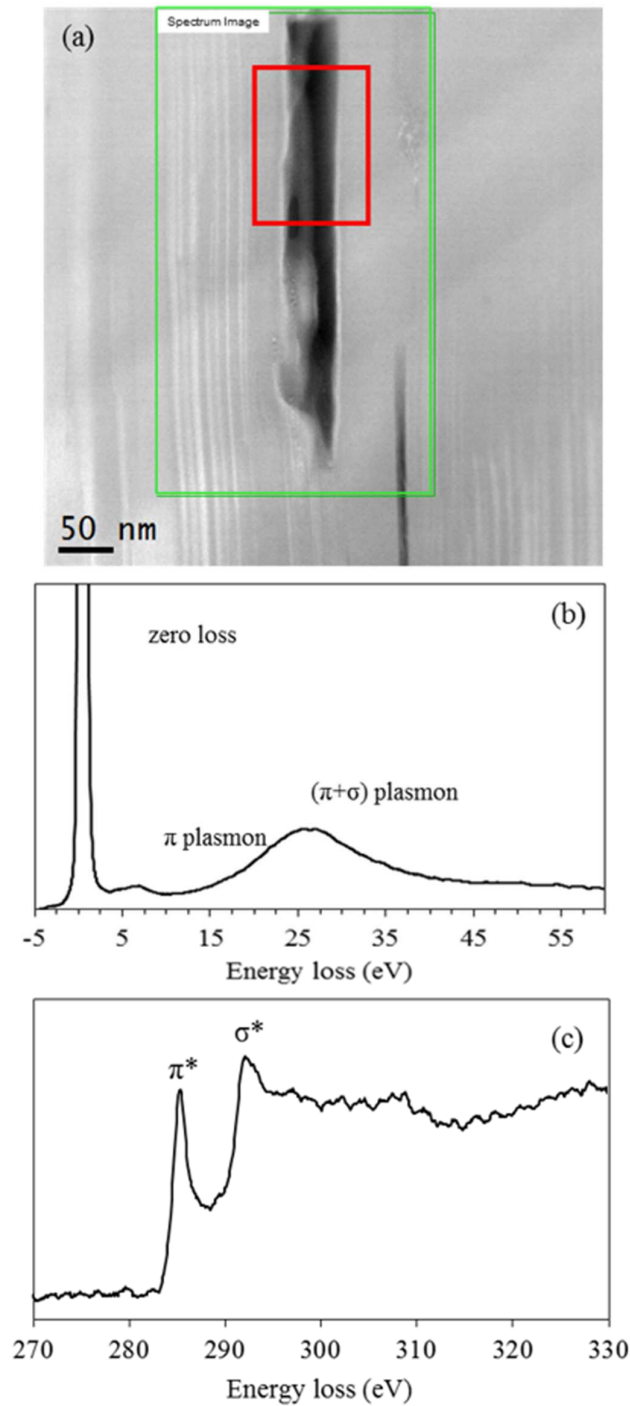


Figure 8 HAADF and EELS spectrum images in BEPO16 with extracted low and core loss EELS. This particular microcrack has a width of ca. 55nm. (a) HAADF image showing the area overview; the spectrum image of the region of interest is

outlined by the green rectangle and the low loss and core loss EELS spectrum images were analysed from the region within the red box. Vertically integrated EEL spectra from the bulk are plotted in (b) for low loss and in (c) for background subtracted core loss.

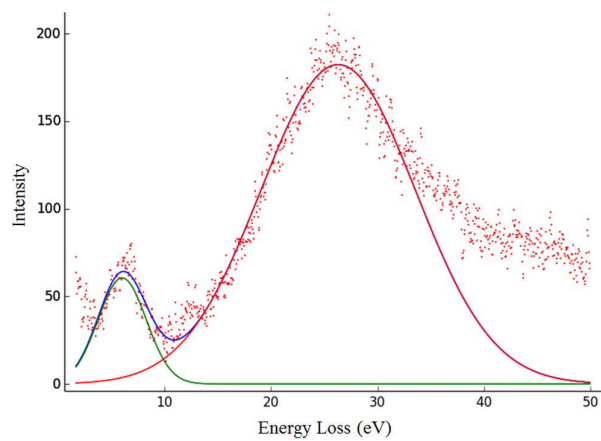


Figure 9 Gaussian fits (green and red) over raw (red dotted) low loss EELS data using HyperSpy.

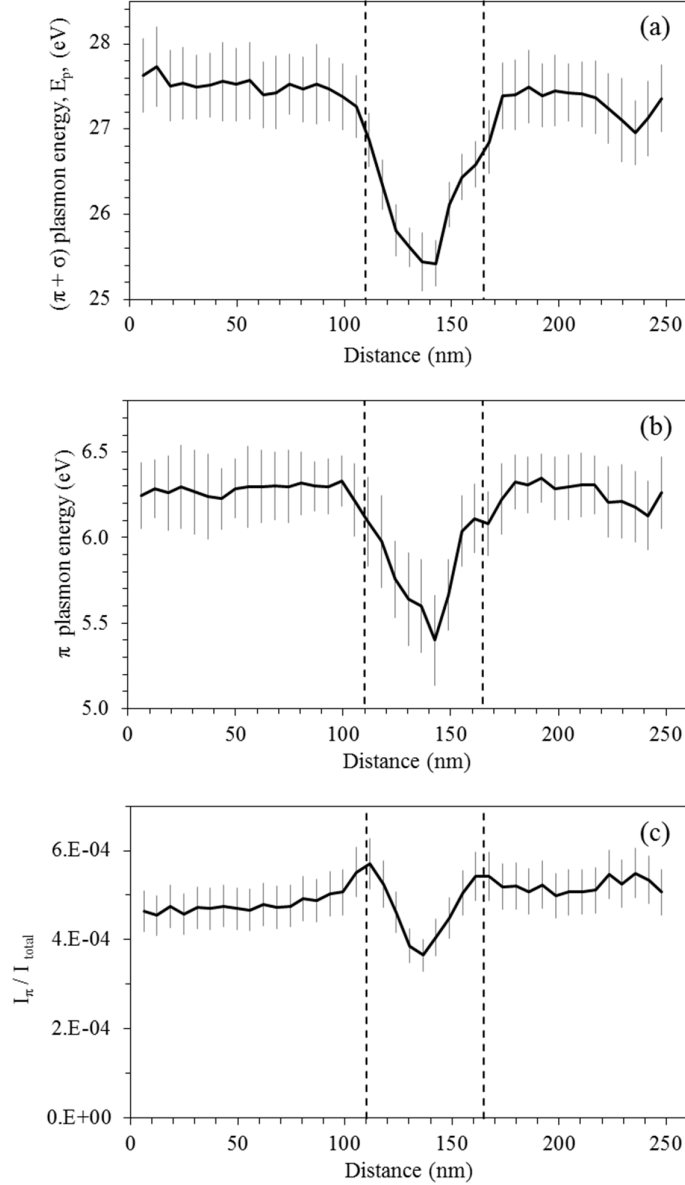


Figure 10 Extracted data from the low loss EEL spectra from the region of interest outlined in red in Figure 8(a). (a) Change in $(\pi+\sigma)$ plasmon energy with distance across crack; (b) change in π plasmon energy with distance across crack; (c) Change in π plasmon intensity with distance across crack, normalised to total low loss (inc. elastic peak). The vertical dotted lines represent the crack boundaries. Error bars represent the standard deviations of the vertically integrated horizontal line scans.

Six areas were examined in BEPO16 and BEPO20. The extracted data from the low loss EEL spectra from the region of interest outlined in red in Figure 8(c) is shown in Figure 10. In the bulk, the $(\pi+\sigma)$ plasmon energy was measured to be between 26.2eV and 27.7eV which is characteristic of near-perfect graphite [17,32,33]. This is also consistent with the findings in [11] where a significant change in $(\pi+\sigma)$ plasmon energy in the bulk due to irradiation was not observed. The energy of the $(\pi+\sigma)$ plasmon peak decreased over all cracks but to differing degrees. The most extreme case was seen in BEPO20 where

the plasmon energy was measured to be 21.5eV at the crack centre; on average the plasmon energy over a microcrack decreased to ca. 23.8eV. For comparison the value for amorphous carbon is ca. 22eV [33,34]. These results show slightly lower values for ($\pi+\sigma$) plasmon energy than those found from EFTEM data, which could be due to the differing collection angles, however the trends are the same. In addition, the possibility of a change in relative sample thickness would also slightly affect the measured plasmon peak energies. The ($\pi+\sigma$) plasmon energy (E_p) is related to the density (N) by:

$$E_p = \frac{h}{2\pi} \left(\frac{Ne^2}{m_0\epsilon_0} \right)^{0.5}$$

so that the observed reduction in ($\pi+\sigma$) plasmon energy across a crack represents a reduced density of material within the cracks [35] (h : Plank's constant, e : electron charge; m_0 : electron rest mass, ϵ_0 : vacuum permittivity). This reduction in density is not seen in bulk irradiated graphite [11] which implies that the contents of the crack are a result of atomic diffusion into the crack and not the remains of an ordered graphite structure.

The π plasmon peak energy also reduced in value across the crack in all areas examined. In the bulk, the π plasmon energy was measured to be between 6.0eV and 6.3eV which is again characteristic of near-perfect graphite [32,33]. In all cases, the reduction in π plasmon energy was to ca. 5 ± 0.5 eV suggesting a reduction in crystallinity and density possibly due to sub 10nm crystallite sizes [36]. The normalised intensity of the π plasmon peak was also measured; a π plasmon window from 4.5eV to 8eV and total intensity window from -3eV to 50eV were used. The intensity was found to reduce by an average of 40% relative to the bulk, which indicates a reduction in the degree of π bonding. These results are in line with those from polycrystalline graphite in [36] where a correlation between π plasmon energy and relative intensity was also found; and with results from a graphitization series in [18] where EELS spectra from pre-graphitized material show a π plasmon intensity of ca. 50% of that in the graphitized product.

In the core loss region, the π^* and σ^* peaks, and the Gaussian associated with changes in intensity of the high energy shoulder of the π^* peak (at ca. 287eV) were analysed using HyperSpy [31]. Both these measured fitted peak intensities were normalised to the total carbon K-edge intensity (integrating over a ca. 20 eV window). A fitting of a typical carbon K-edge using Gaussian peaks (G1 to G5, as labelled) is shown in Figure 11. All five core loss Gaussians were fitted using the following constraints:

- G1 centred at ca. 284.5eV (with a constraint on the FWHM (β): $0.25\text{eV} \leq \beta \leq 2\text{eV}$);
- G2 centred at ca. 286.45eV ($0.2\text{eV} \leq \beta \leq 4.0\text{eV}$)
- G3 centred at ca. 288.25eV ($0.2\text{eV} \leq \beta \leq 4.0\text{eV}$).
- G4 centred at ca. 291.25eV ($2.1\text{eV} \leq \beta \leq 3.0\text{eV}$);

- G5 centred at ca. 296.75eV ($11.2\text{eV} \leq \beta \leq 13.1\text{eV}$).

Full details of this analysis method can be found in [11]. However, briefly, the relative intensity under G1 is assumed to represent the proportion of planar sp^2 bonded carbon, as found in pristine graphite, whereas the combined relative areas under G2 and G3 represent the proportion of *non-planar* sp^2 bonded carbon, similar to that found in fullerenes. In previous studies [11,18,19] these relative intensities have been normalised to reference materials, such as HOPG and crystalline C_{60} , in order to obtain absolute values. However in this case we simply report the relative change in Gaussian peak areas as the STEM probe traverses the region of interest, from bulk to crack. These results are displayed in Figure 12 which shows evidence for the direct replacement of planar sp^2 bonding by *non-planar* sp^2 (through the introduction of non-hexagonal rings and the fragmentation of basal planes) in the disordered graphitic material found within a crack. This is demonstrated by the fact that across all regions examined for both BEPO16 and BEPO20, within the crack the planar sp^2 content decreased by an average of ca. 33% ($\sigma_{\bar{x}} = 18\%$) while the *non-planar* sp^2 content increased by an average of ca. 30% ($\sigma_{\bar{x}} = 15\%$) relative to the surrounding bulk material.

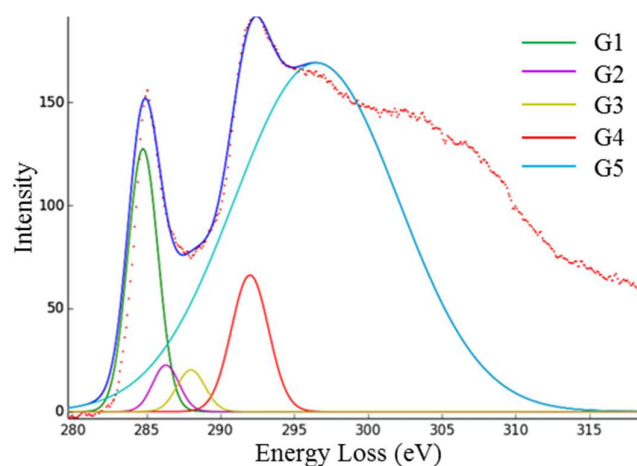


Figure 11 Five Gaussian fits (green, purple, yellow, red, and turquoise) over raw (red dotted) core loss EELS data (background subtracted) using HyperSpy.

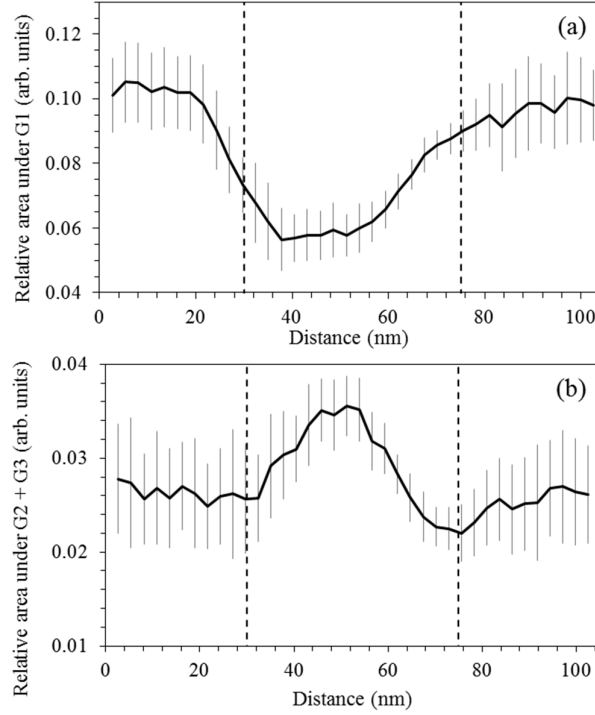


Figure 12 Extracted data from the core loss EEL spectra from the region of interest outlined in red in Figure 8(a). (a) Change in relative area under G1 (associated with planar sp^2 content) with distance across crack. (b) Change in relative area under G2 + G3 (associated with *non-planar* sp^2 content) with distance across crack. The vertical dotted lines represent the crack boundaries. Error bars represent the standard deviations of the vertically integrated horizontal line scans.

4. Discussion and Conclusions

TEM imaging of a set of nuclear graphites irradiated at different doses (but low temperatures) has shown the number of microcracks within the material increased with increasing dose, fragmenting the crystalline microstructure into smaller nanocrystalline regions. This is in agreement with the Raman spectroscopy data for these samples, measured by Krishna *et al.* [12] who observed that the ratio between the intensities of the D and G Raman peaks (I_D/I_G ratio) and the width of the G peak both increased with increasing neutron dose. The change in I_D/I_G ratio was attributed to a change in crystallite dimension, L_a , which was calculated to be 60% smaller in BEPO20 as compared to the low dose BEPO1 specimen using the relationship of Tuinstra and Koeing [37]. HRTEM image analysis showed that in irradiated specimens, the graphite basal planes in the bulk material appeared to be shorter in length and of an increased tortuosity, but with no observed relation to received dose. This is in agreement with the Raman data, where analysis of the broadening G peak was related to an increase in the degree of turbulence and disordering of basal planes [12].

For the regions investigated, all microcracks of width <100nm were either fully or partially filled with low density material in agreement with the study of Wen *et al.* [6] on unirradiated and Karthik *et*

al. [9] on irradiated nuclear graphite materials. From EELS and EDX measurements we found this material to be composed of low density carbon and of reduced graphitic character. Comparing the surrounding bulk material to the material within the cracks in irradiated specimens, EELS revealed a reduction in the volume plasmon energy within the microcracks consistent with a lower density material, together with a 30% reduction in planar sp^2 bonded carbon which was replaced by *non-planar* sp^2 bonded carbon. The degree of structural change of the bulk material was not observed to vary with respect to received dose. In material surrounding the microcracks in irradiated specimens, EFTEM measurements revealed a ca. 8nm periodic change in graphitic character, which was tentatively assigned to the beginnings of microcrack formation, where a region of low graphitic character will widen to form a microcrack containing disordered carbon.

The presence of disordered graphitic material within microcracks before irradiation potentially has implications for the evolution of the material within these microcracks and also the mechanisms behind dimensional change around microcracks during neutron irradiation. The accommodation by microcracks of *c*-axis expansion of graphite crystals during irradiation, discussed in the introduction, could be significantly affected by the presence of lower density material within the crack preventing crack closure either partially or totally.

The origin of disordered material within cracks of unirradiated specimens is not addressed in the literature, although it is possible that the material be a result of incomplete graphitization or the presence of quinolone-insolubles (QI) (which are higher in coal-tar pitches as opposed to petroleum based pitches [9]). However Karthik reports QI occurs as particles within the binder regions of the nuclear graphite microstructure [9], but that is not to say this disordered material is not mobile. Note that it is not expected that the low temperature annealing (ca. 230°C) of the BEPO graphite would cause significant restructuring of either the bulk graphite or the material within the cracks. An alternative explanation could be that the cleavage microcracks, created as a result of anisotropic thermal expansion/contraction, act as sinks for irradiation induced defects – filling with disordered carbon as defects cluster and segregate at these low energy sites. However, the migration energy of a single vacancy is such that it only becomes mobile above an irradiation temperature of 180°C, and this is predicted to be even higher for a single interstitial defect [28]. This initially suggests that the disordered material observed within the cracks does not accumulate as a direct result of migration of irradiation-induced defects, however as discussed previously, the low basal surface energy barrier and the irradiation-induced fragmentation of the microstructure creates increased possibilities for fast diffusion pathways via surfaces and grain boundaries.

If the microcracks do act as diffusion sinks for irradiation-induced defects, then we might expect the total amount of disordered material within the cracks to increase gradually with increasing dose. Although we tentatively suggest that the areal concentration of cracks does increase with dose, we have

no direct evidence for the total amount of disordered carbon material similarly increasing. Admittedly the increase in the Raman I_D/I_G ratio could be due (at least partially) to an increase in the total amount of disordered material in cracks, as well as the result of a decrease in crystallite size due to fragmentation of the microstructure.

In order to resolve this discussion, a further much more quantitative and detailed analysis of the in-crack material within non-irradiated specimens and irradiated specimens at a range of temperatures is required. In-crack material structure and behaviour following high temperature ($>2000^\circ\text{C}$) annealing would also be of interest. Notwithstanding, the presence of low density material within microcracks has implications for the understanding of radiation-induced dimensional change and the associated changes in properties of nuclear graphite during service life. The characterisation technique could be extended beyond nuclear graphite and applied to a wide range of carbon materials.

Acknowledgments

Funding was provided by the National Nuclear Laboratory and EPSRC (EP/J502042/1, EP/I003169/1). We gratefully acknowledge the Leeds EPSRC Nanoscience and Nanotechnology Facility (grant EP/K023853/1) for TEM and SAED. We thank Jean-Pierre Da Costa and the late Patrick Weisbecker for provision of the HRTEM analysis software through the program ‘‘PyroMaN’’ (grant ANR-BLAN-2010-0929) supported by the ANR agency. Fred S. Hage would like to acknowledge Magnus Kristofer Nord (Norwegian University of Science and Technology, Trondheim, Norway) for assistance and useful discussions when setting up the carbon low loss and carbon-K edge fitting procedures in HyperSpy (freely available from <http://hyperspy.org/>). SuperSTEM is the UK Engineering and Physical Sciences Research Council (EPSRC) National Facility for aberration-corrected STEM. The views expressed are those of the authors and do not necessarily represent those of the funding bodies.

References

- [1] Yan P, Delannay L, Payne JFB, Tzelepi A. A Micromechanistic Crystal Plasticity Model for Graphite. 4th EDF Energy Nucl. Graph. Symp. Eng. Challenges Assoc. with Life Graph. React. Cores, EMAS Publishing; 2014.
- [2] Sutton AL, Howard VC. The role of porosity in the accommodation of thermal expansion in graphite. *J Nucl Mater* 1962;1:58–71. doi:10.1016/0022-3115(62)90194-0.

- [3] Hacker PJ, Neighbour GB, McEnaney B. The coefficient of thermal expansion of nuclear graphite with increasing thermal oxidation. *JPhys D ApplPhys* 2000;33:991–8. doi:0022-3727/00/080991+08.
- [4] Mrozowski S. Mechanical Strength, Thermal Expansion and Structure of Cokes and Carbons. *Proc Conf Carbon* 1954:31.
- [5] Delannay L, Yan P, Payne JFB, Tzelepi A. Predictions of inter-granular cracking and dimensional changes of irradiated polycrystalline graphite under plane strain. *Comput Mater Sci* 2014;87:129–37. doi:10.1016/j.commat.2014.02.008.
- [6] Wen K, Marrow J, Marsden B. Microcracks in nuclear graphite and highly oriented pyrolytic graphite (HOPG). *J Nucl Mater* 2008;381:199–203. doi:10.1016/j.jnucmat.2008.07.012.
- [7] Hall G, Marsden BJ, Fok SL. The microstructural modelling of nuclear grade graphite. *J Nucl Mater* 2006;353:12–8. doi:10.1016/j.jnucmat.2006.02.082.
- [8] Hinks JA, Jones AN, Theodosiou A, van den Berg JA, Donnelly SE. Transmission Electron Microscopy Study of Graphite under in situ Ion Irradiation. *J Phys Conf Ser* 2012;371:012046. doi:10.1088/1742-6596/371/1/012046.
- [9] Karthik C, Kane J, Butt DP, Windes WE, Ulic R. Neutron irradiation induced microstructural changes in NBG-18 and IG-110 nuclear graphites. *Carbon N Y* 2015;86:124–31. doi:10.1016/j.carbon.2015.01.036.
- [10] Karthik C, Kane J, Butt DP, Windes WE, Ulic R. In situ transmission electron microscopy of electron-beam induced damage process in nuclear grade graphite. *J Nucl Mater* 2011;412:321–6. doi:10.1016/j.jnucmat.2011.03.024.
- [11] Mironov BE, Freeman HM, Brown AP, Hage FS, Scott AJ, Westwood AVK, et al. Electron irradiation of nuclear graphite studied by transmission electron microscopy and electron energy loss spectroscopy. *Carbon N Y* 2015;83:106–17. doi:10.1016/j.carbon.2014.11.019.

- [12] Krishna R, Jones AN, Mcdermott L, Marsden BJ. Neutron irradiation damage of nuclear graphite studied by high-resolution transmission electron microscopy and Raman spectroscopy. *J Nucl Mater* 2015;467:557–65. doi:10.1016/j.jnucmat.2015.10.027.
- [13] Bell JC, Bridge H, Cottrell AH, Greenough GB, Reynolds WN, Simmons JHW. Stored Energy in the Graphite of Power-Producing Reactors. *Philos Trans R Soc A Math Phys Eng Sci* 1962;254:361–95. doi:10.1098/rsta.1962.0002.
- [14] Huntingdon S, Ormerod P, Mowles S. Characterisation of Oxidised and Irradiated Magnox Core Graphite. 2002.
- [15] Wise M. Management of UKAEA graphite liabilities. Harwell, Didcot, Oxfordshire: 2001. doi:IAEA-NGWM/CD--01.
- [16] Brydson R. Electron Energy Loss Spectroscopy. Oxford, UK: Royal Microscopical Society Microscopic Handbooks Volume 48. BIOS Scientific Publishers Ltd; 2001.
- [17] Daniels HR, Brydson R, Brown A, Rand B. Quantitative valence plasmon mapping in the TEM: viewing physical properties at the nanoscale. *Ultramicroscopy* 2003;96:547–58. doi:10.1016/S0304-3991(03)00115-3.
- [18] Daniels H, Brydson R, Rand B, Brown A. Investigating carbonization and graphitization using electron energy loss spectroscopy (EELS) in the transmission electron microscope (TEM). *Philos Mag* 2007;87:4073–92. doi:10.1080/14786430701394041.
- [19] Zhang Z, Brydson R, Aslam Z, Reddy S, Brown A, Westwood A, et al. Investigating the structure of non-graphitising carbons using electron energy loss spectroscopy in the transmission electron microscope. *Carbon N Y* 2011;49:5049–63. doi:10.1016/j.carbon.2011.07.023.
- [20] Mironov BE. Nuclear Graphite: Structural Characterisation and the Effects of Irradiation (Ph.D Thesis). University of Leeds, 2015.

- [21] Muto S, Tanabe T. Temperature effect of electron-irradiation-induced structural modification in graphite. *J Nucl Mater* 2000;283-287:917–21. doi:10.1016/S0022-3115(00)00117-3.
- [22] Gallego NC, Meisner RA, Burchell TD. Annealing Studies of Irradiated HOPG using X-ray Measurements. Present. Int. Nucl. Graph. Spec. Meet., Seattle: Oak Ridge National Laboratory; 2013.
- [23] Schaffer M, Schaffer B, Ramasse Q. Sample preparation for atomic-resolution STEM at low voltages by FIB. *Ultramicroscopy* 2012;114:62–71. doi:10.1016/j.ultramic.2012.01.005.
- [24] DaCosta JP, Weisbecker P, Farbos B, Leyssale J-M, Vignoles GL, Germain C. Investigating carbon materials nanostructure using image orientation statistics. *Carbon* N Y 2015;84:160–73. doi:10.1016/j.carbon.2014.11.048.
- [25] DaCosta JP, Germain C, Baylou P. Spectral characterization of orientation data along curvilinear structures. ICPR2, 2004.
- [26] Thrower PA, Mayer RM. Point defects and self-diffusion in graphite. *Phys Status Solidi* 1978;47:11–37. doi:10.1002/pssa.2210470102.
- [27] Gulans A, Krasheninnikov A, Puska M, Nieminen R. Bound and free self-interstitial defects in graphite and bilayer graphene: A computational study. *Phys Rev B* 2011;84:1–6. doi:10.1103/PhysRevB.84.024114.
- [28] Trevethan T, Dyulgerova P, Latham CD, Heggie MI, Seabourne CR, Scott AJ, et al. Extended Interplanar Linking in Graphite Formed from Vacancy Aggregates. *Phys Rev Lett* 2013;111:095501. doi:10.1103/PhysRevLett.111.095501.
- [29] Zhang H, Zhao M, Yang X, Xia H, Liu X, Xia Y. Diffusion and coalescence of vacancies and interstitials in graphite: A first-principles study. *Diam Relat Mater* 2010;19:1240–4. doi:10.1016/j.diamond.2010.06.010.
- [30] Telling RH, Ewels CP, El-Barbary AA, Heggie MI. Wigner defects bridge the graphite gap. *Nat Mater* 2003;2:333–7. doi:10.1038/nmat876.

- [31] Peña F de la, Burdet P, Ostasevicius T, Sarahan M, Nord M, Fauske VT, et al. HyperSpy 0.8.1 2015. doi:10.5281/zenodo.27735.
- [32] Fink J, Muller-Heinzerling T, Pfluger J, Scheerer B. Investigation of hydrocarbon-plasma-generated carbon films by electron-energy-loss spectroscopy. *Phys Rev B* 1984;30:4713–8. doi:http://dx.doi.org/10.1103/PhysRevB.30.4713.
- [33] Chu PK, Li L. Characterization of amorphous and nanocrystalline carbon films. *Mater Chem Phys* 2006;96:253–77. doi:10.1016/j.matchemphys.2005.07.048.
- [34] Praver S, Rossouw CJ. Structural investigation of helium ion-beam-irradiated glassy carbon. *J Appl Phys* 1988;63:4435–9. doi:10.1063/1.340162.
- [35] Egerton RF. *Electron Energy-Loss Spectroscopy in the Electron Microscope*. 3rd ed. Springer; 2011.
- [36] Hashimoto H, Nishiuma S, Takada K, Nakamura K, Ueno R, Den T. Crystallite Size Dependence of Plasmon Energies in Polycrystalline Graphite Observed by Reflected Electron Energy Loss Spectroscopy. *Jpn J Appl Phys* 1999;38:4136–41. doi:10.1143/JJAP.38.4136.
- [37] Tuinstra F, Koenig JL. Raman Spectrum of Graphite. *J Chem Phys* 1970;53:1126. doi:10.1063/1.1674108.